Eur. Phys. J. Special Topics **150**, 177–182 (2007)

DOI: 10.1140/epjst/e2007-00297-1

THE EUROPEAN PHYSICAL JOURNAL SPECIAL TOPICS

Nuclear structure of neutron-rich nuclei near closed shells from excited-state g-factor measurements

A.E. Stuchbery[1] and P.F. Mantica[2]

[1] Department of Nuclear Physics, The Australian National University, Canberra, ACT 0200, Australia
[2] National Superconducting Cyclotron Laboratory, Michigan State University, East Lansing, MI 48824, USA and Department of Chemistry, Michigan State University, East Lansing, MI 48824, USA

Received: January 31, 2007

Abstract. New techniques to measure the g factors of picosecond-lived excited states of neutron-rich nuclei produced as radioactive beams are discussed along with their applications to study nuclear structure near $^{132}_{50}Sn_{82}$ and in the region between $N = 20$ and $N = 28$.

PACS. 21.10.Ky Electromagnetic moments – 25.70.De Coulomb excitation – 23.20.En Angular distribution and correlation measurements – 21.60.Cs Shell model – 27.30.+t $20 \leq A \leq 40$ – 27.60.+j $90 \leq A \leq 149$

1 Introduction

The magnetic moment is a key observable to probe the single-particle structure of a nuclear state. In the quest to understand the novel structures being found in neutron-rich nuclei, it is important to develop techniques for g factor measurements on picosecond-lived excited states of exotic isotopes produced as radioactive beams. Great progress has been made recently. In this paper we discuss two newly developed techniques to study the structure of neutron-rich nuclei. In the first case, the Recoil In Vacuum (RIV) technique has been used to measure excited-state g factors in neutron-rich nuclei near ^{132}Sn produced by the ISOL method [1]. In the second case, a High-Velocity Transient-Field (HVTF) technique has been applied to neutron-rich sulfur isotopes between $N = 20$ and $N = 28$ produced as fast fragment beams [2].

2 Recoil in vacuum (RIV) near $^{132}_{50}Sn_{82}$

When a free ion moves through vacuum, the hyperfine interaction couples the atomic spin $\boldsymbol{J}$ to the nuclear spin $\boldsymbol{I}$ and together they precess about the total spin $\boldsymbol{F} = \boldsymbol{I} + \boldsymbol{J}$, as illustrated in figure 1 (left panel). The precession frequency $\omega_{F,F'}$ is proportional to the nuclear g factor and the magnitude of the hyperfine magnetic field at the nucleus. To measure the g factor, the nuclear state of interest is excited by a suitable reaction and then allowed to recoil into vacuum. The effect of the hyperfine interaction is observed via the perturbation of the angular correlation/distribution of the γ-rays de-exciting the state.

Recoil-in-vacuum (RIV) can refer to two quite distinct experimental techniques, depending on whether the ion has a very simple, few-electron configuration, or whether it has a complex many-electron configuration [3]. We have proposed [4] a version of the RIV technique to measure the first-excited state g factors of H-like light ions ($Z < 20$) produced by fast fragmentation. This technique is still under development. Here we focus on the successful application of the RIV technique to slower-moving many-electron radioactive ions produced by the ISOL method [1]. In many cases, the RIV technique, which determines the magnitude of the g factor, might not be chosen over the transient-field technique [5], which can determine the sign; however RIV with ISOL-type radioactive beams has a number of advantages [1], not least being that $|g|$ can be determined from the same data set as the $B(E2)$.

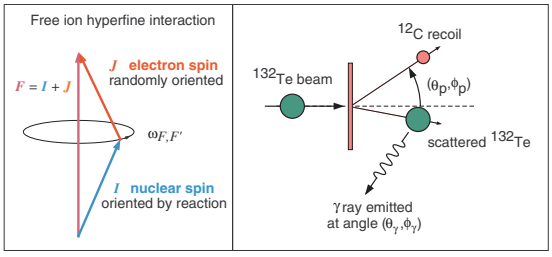

Fig. 1. Left: The free-ion hyperfine interaction on which the Recoil in Vacuum technique is based. Right: Reaction kinematics for the ^{132}Te g-factor measurement.

The experiments were performed at the Holifield Radioactive Ion Beam Facility (HRIBF) at Oak Ridge National Laboratory. Radioactive beams of ^{132}Te at an energy of 3 MeV/nucleon were incident on a carbon foil target as illustrated in the right panel of figure 1. The first-excited state of ^{132}Te was Coulomb excited in inverse kinematics at an energy well below the Coulomb

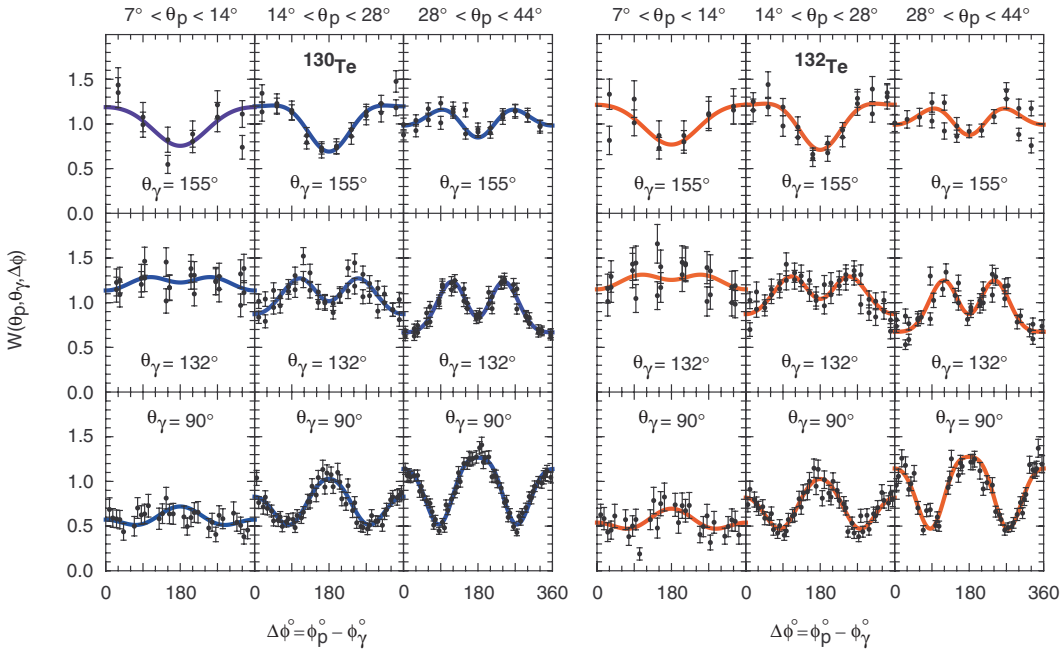

Fig. 2. Angular correlations perturbed by free-ion hyperfine fields for stable ^{130}Te and neutron-rich ^{132}Te.

barrier, which ensures negligible multiple excitation. The ^{132}Te ions exit the target with an average velocity of $v/c = 6.26\%$.

Recoiling ^{12}C ions were detected in the HYBALL array while coincident γ-rays de-exciting ^{132}Te were detected in CLARION [6]. The relative efficiencies of the HYBALL particle detectors were determined from the simultaneously observed Rutherford scattering rate. A new feature of this RIV measurement was the exploitation of the azimuthal segmentation of the HYBALL and CLARION arrays, coupled with a detailed quantitative analysis of the azimuthal angular correlations.

The ^{12}C-γ angular correlation is given by

$$W(\theta_p, \theta_\gamma, \Delta\phi) = \sum_{kq} B_{kq}(\theta_p) Q_k G_k F_k D^{k*}_{q0}(\Delta\phi, \theta_\gamma, 0), \quad (1)$$

where the angles are defined in figure 1 and $\Delta\phi = \phi_p - \phi_\gamma$. B_{kq} is the statistical tensor, which specifies the spin alignment of the initial state; F_k is the usual F-coefficient for the γ-ray transition. G_k, the vacuum deorientation attenuation factor, contains the information about the nuclear g factor. Q_k is the attenuation factor for the finite size of the γ-ray detector and D^k_{q0}, the rotation matrix, is proportional to a spherical harmonic. Further details of the angular correlation formalism may be found in [7], for example. The statistical tensors B_{kq} were evaluated using the program CHAD (Clarion-Hyball Angular Distributions) [8], which performs the required integrations over the energy loss of the beam in the target and over the trapezoidal faces of the HYBALL detectors. CHAD uses the de Boer-Winther Coulomb excitation code [9] as a subprogram.

If the coincidence count rate in a chosen pair of particle and γ-ray detectors, $N(\theta_p, \theta_\gamma, \phi_{p_i} - \phi_\gamma)$, is normalized to the coincidence rate summed over all of the particle detectors in the particular HYBALL ring, the unperturbed angular correlations can be calculated with no free parameters. In other words, this normalization procedure factors out the γ-ray detection efficiency, giving

$$\frac{N(\theta_p, \theta_\gamma, \phi_{p_i} - \phi_\gamma)}{\sum_i N(\theta_p, \theta_\gamma, \phi_{p_i} - \phi_\gamma)} = \frac{W(\theta_p, \theta_\gamma, \phi_{p_i} - \phi_\gamma)}{N_H W(\theta_p, \theta_\gamma)}, \quad (2)$$

where N_H is the number of detectors in the HYBALL ring and $W(\theta_p, \theta_\gamma)$ is given by equation (1) with $q \equiv 0$. By this procedure, the only free parameters required to fit the perturbed angular correlations are the vacuum attenuation factors, G_2 and G_4. Note that the experiments determine the time-integral attenuation factors,

$$G_k(\infty) = \int_0^\infty G_k(t) \exp(-t/\tau) dt/\tau, \quad (3)$$

where τ is the mean life of the nuclear state.

Since there is an ensemble of many-electron ions with a wide distribution of electron configurations, there is a superposition of many hyperfine frequencies, which gives a quasi-exponential time dependence to the vacuum attenuation factors, $G_k(t)$. Thus the alignment of the nuclear state, and hence the anisotropy of the γ-ray angular correlation, decreases approximately exponentially with time, at a rate that depends on the magnitude of the nuclear g factor. Since the interaction is complex, and impossible to calculate from first principles, a calibration using stable isotopes with known g factors and level lifetimes is essential. Calibration measurements on stable beams of ^{122,126,130}Te with energies of 3 MeV/nucleon were used for this purpose. Figure 2 shows the perturbed angular correlations for ^{130}Te and ^{132}Te. It can be seen by inspection that the vacuum attenuation is similar for these two isotopes.

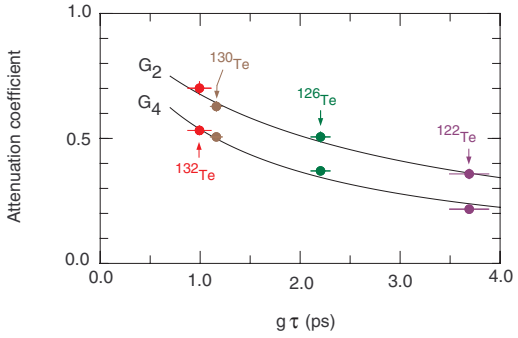

Fig. 3. Attenuation factors for the Te isotopes. The solid line is the fit from which $g(2^+)$ in ^{132}Te was determined.

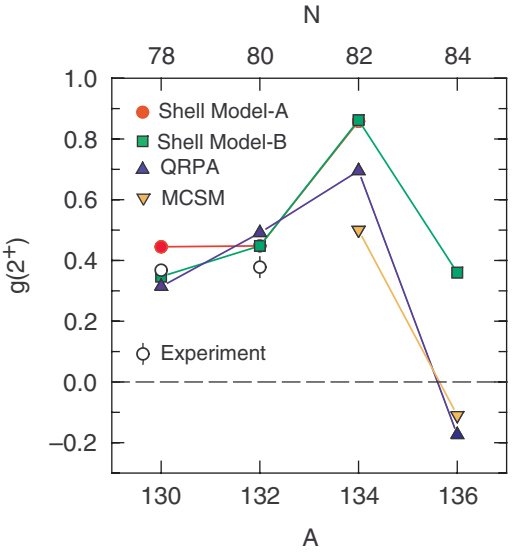

Fig. 4. Theoretical g factors in the Te isotopes compared with experiment. Shell model calculations A and B are from [12,13], respectively. QRPA is from [14] and MCSM from [15].

Figure 3 illustrates the procedure used to determine $g(2_1^+)$ in ^{132}Te from the calibration data on ^{122,126,130}Te. The measured G_k values are plotted versus the product $g\tau$, which was evaluated using a new set of relative g factors for the stable isotopes, measured precisely at the Australian National University [10]. The line is an empirical fit assuming $G_k(t) = \exp(-|g|t/C_k)$, where C_2, C_4 and $g(2_1^+)$ in ^{132}Te are free parameters. This expression for the attenuation coefficients corresponds to a static electron configuration with a Lorentzian distribution of hyperfine frequencies, but with negligible hard core terms. A full description and a model-based evaluation of the procedure will be presented elsewhere [11].

The experimental g factors in ^{130}Te and ^{132}Te are compared with theoretical predictions in figure 4. Most of the theories predict a quite pronounced increase in g factor for ^{132}Te, compared with ^{130}Te, which is not found experimentally. As shown in figure 5, however, the experimental g factor of ^{132}Te fits well with the $g(2^+)$ systematics in the $A \sim 130$ region, and has a comparable magnitude to those in the neighboring $N = 80$ isotones of Xe and Ba. This

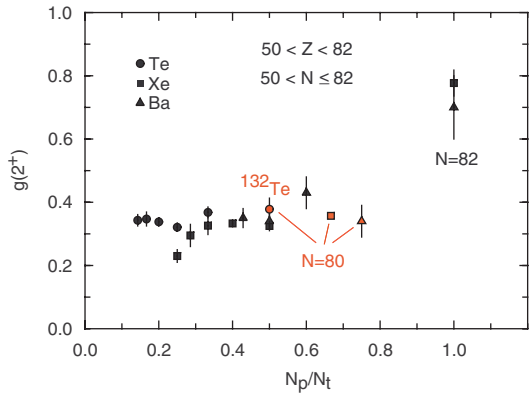

Fig. 5. $g(2_1^+)$ systematics in the $A \sim 130$ region. Experimental g factors (see [10,12,18] and references therein) are plotted versus the valence proton fraction, N_p/N_t, which is defined as in the Interacting Boson Model [19].

agreement with the systematics gives confidence in the technique. Beam time has been approved to study the radioactive nuclei ^{134}Te and ^{136}Te, where there are conflicting theoretical predictions for the g factors (figure 4). The case of ^{136}Te is of particular interest. At the microscopic level $g \sim Z/A$, as obtained by one of the shell model studies [13], is associated with strong coupling between the proton and neutron orbits. In conflict with this picture, the quasiparticle random phase approximation (QRPA) [14] and Monte Carlo shell model (MCSM) [15] calculations have weakly coupled proton and neutron excitations such that the 2_1^+ state is predominantly a neutron excitation ($g \sim -0.1$), while the 2_2^+ state is predominantly a proton excitation. The RIV g factor measurement on ^{136}Te is expected to be able to distinguish between these competing theoretical pictures, even though the radioactive beam intensity is two orders of magnitude weaker than for ^{132}Te. It is interesting to note that in the stable $N = 84$ nuclei ^{142}Ce and ^{144}Nd, the $g(2_1^+)$ values are clearly positive, although reduced to about $0.5Z/A$ [16,17].

3 High-velocity transient-field (HVTF) technique: ^{38}S and ^{40}S

The first application of a high-velocity transient-field technique [20] to measure the g factors of excited states of neutron-rich nuclei produced as fast radioactive beams was reported recently [2]. Questions on the nature and origins of deformation between $N = 20$ and $N = 28$ were addressed by measuring the g factors of the 2_1^+ states in $^{38}_{16}S_{22}$ and $^{40}_{16}S_{24}$.

The experiment was conducted at the Coupled Cyclotron Facility of the National Superconducting Cyclotron Laboratory (NSCL) at Michigan State University. Beams of ^{38}S and ^{40}S with energies of 40 MeV/nucleon were made incident, in turn, upon a target consisting of contiguous layers of Au and Fe, 355 mg/cm^2 thick and 110 mg/cm^2 thick, respectively. The nuclear state of interest was excited and aligned by

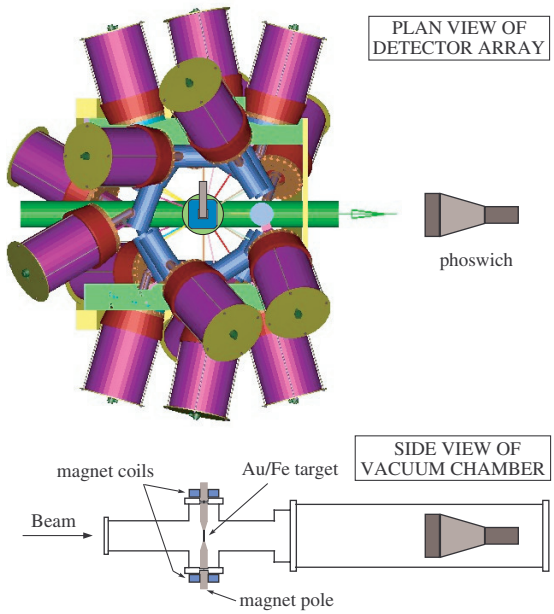

Fig. 6. Apparatus used in the high-velocity transient-field measurements at NSCL. Overhead and side views of the SeGA detectors and the target chamber show the magnet, target and phoswich detector.

intermediate-energy Coulomb excitation on the Au layer of the target. Within the Fe layer, the excited nucleus was subjected to the transient field in a higher velocity regime than has been used previously for moment measurements. The effect of the transient field is to cause the nuclear spin to precess. The nuclear precession angle, to which the g factor is proportional, was observed via the perturbed angular correlation of the de-excitation γ-rays, measured using the Segmented Germanium Array (SeGA).

Figure 6 shows the experimental arrangement. The target was held between the pole tips of a compact electromagnet that provided a magnetic field of 0.11 T, sufficient to fully magnetize the Fe layer. To minimize possible systematic errors, the external magnetic field was automatically reversed every 600 s. Projectiles scattered forward out of the target were detected by a phoswich detector placed downstream of the target position. The maximum scattering angle accepted by the phoswich detector, 5.5°, limited the distance of closest approach to be near the nuclear interaction radius in both the Au and Fe target layers.

Comparisons between the experimental and theoretical (unperturbed) angular correlations are made in figure 7. Precession angles were determined from field-up/field down ratios by standard procedures [2,21]. The g factors were then extracted from the measured precession angles using a high-velocity transient-field parametrization [20]. In figure 8 the experimental results are compared with stable-beam measurements on their isotones. The statistical uncertainties on the radioactive beam measurements rival those on the stable beam studies. This precision is made possible by use of the fast beams and a thick ferromagnetic layer, which produces

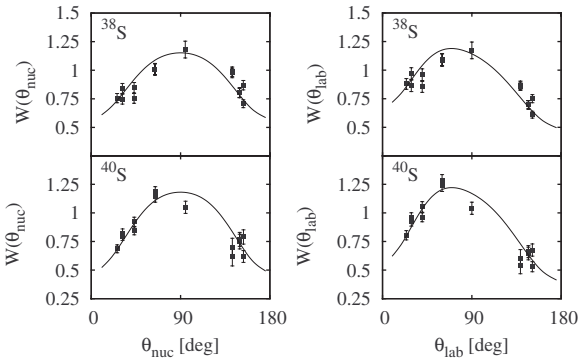

Fig. 7. Angular correlations for ^{38}S and ^{40}S. The left panels show the angular correlation in the frame of the projectile nucleus, while the right panels show the same angular correlations in the lab frame. Data are normalized to the calculated angular correlation.

a precession angle (per unit g factor) that is an order of magnitude larger than those obtained in the stable beam measurements at low velocity. Further details of the experiments are presented elsewhere [2,21].

Shell model calculations were performed using the code OXBASH [25] and the *sd-pf* model space where (for $N \geq 20$) valence protons are restricted to the *sd* shell and valence neutrons are restricted to the *pf* shell. The Hamiltonian was that developed in [26] for neutron-rich nuclei around $N = 28$, i.e. the SDPF-NR interaction [27]. These calculations reproduce the energies of the low-excitation states to within 200 keV. With standard effective charges of $e_p \sim 1.5$ and $e_n \sim 0.5$ they also reproduce the measured $B(E2)$ values. Table 1 shows the experimental and theoretical $B(E2)$ and quadrupole moment values in terms of the equivalent deformation parameter, β.

The g factors of the 2_1^+ states were evaluated using the bare nucleon g factors. The calculated g factors are compared with experimental results in figure 8 and Table 1; Table 1 also shows the orbital and spin contributions to the g factor originating from both protons and neutrons. Overall the level of agreement between theory and experiment is satisfactory, given that there is extreme

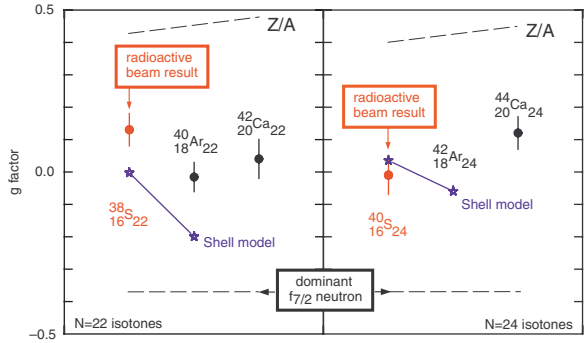

Fig. 8. Measured g factors in ^{38}S and ^{40}S compared with stable-beam measurements on their isotones [22–24] and shell model calculations. Broken lines indicate the collective and single particle limits.

Table 1. Theoretical deformation parameters and g factors compared with experiment.

Nuclide	Model	$\beta_Q^{\rm th}$	$\lvert\beta_{E2}^{\rm th}\rvert$	$\lvert\beta_{E2}^{\rm exp}\rvert$	$g_{\rm proton}^{\rm th}$			$g_{\rm neutron}^{\rm th}$	$g^{\rm th}$	$g^{\rm exp}$
					orbital	spin	total			
$^{38}_{16}S_{22}$	SDPF	+0.17	0.26	0.25(2)	0.225	0.073	+0.298	−0.301	−0.003	+0.13(5)
	SDF	−0.13	0.20		0.087	0.049	+0.136	−0.494	−0.358	
$^{40}_{16}S_{24}$	SDPF	+0.33	0.34	0.28(2)	0.225	0.051	+0.276	−0.241	+0.035	−0.01(6)
	SDF	+0.17	0.28		0.249	0.070	+0.318	−0.404	−0.085	

sensitivity to configuration mixing and a near cancelation of the proton and neutron contributions to the g factors (Table 1).

Many authors have argued on experimental and theoretical grounds that ^{40}S ($N = 24$) is deformed, some linking it to a weakening of the $N = 28$ shell gap (see [28–34] and references therein). To explore the role of excitations across the $N = 28$ shell gap, a further set of calculations was performed in which the neutrons were confined to the $f_{7/2}$ orbit. The results of these calculations, labeled SDF, are also given in Table 1.

Supporting the interpretation that ^{40}S is deformed, the shell model calculations predict consistent intrinsic quadrupole deformations when derived from either the $B(E2)$ or the quadrupole moment, implying a prolate deformation of $\beta \approx +0.3$, in agreement with the value deduced from the experimental $B(E2)$ [28]. The near zero magnetic moment, however, does not conform to the usual collective model expectation of $g \sim Z/A$.

The essential difference between the deformed neutron-rich sulfur isotopes and the deformed nuclei previously encountered (i.e. either light nuclei with $N = Z$ or heavier deformed nuclei) is that the spin contributions to the magnetic moments are relatively more important, especially for the neutrons. It can be seen from Table 1 that the proton contributions to the g factors are dominated by the orbital component, as is usually the case for deformed nuclei, but the substantial neutron contributions originate entirely with the intrinsic spin. The quadrupole collectivity in ^{40}S is therefore not that of a featureless charged liquid drop. Relatively few particles are involved in the collective motion so that, despite considerable configuration mixing, both ^{38}S and ^{40}S retain a dominant occupation of the neutron $f_{7/2}$ orbit, which has $g_{\rm Schmidt} = -0.547$.

The role of neutron excitations across the $N = 28$ shell gap can be examined by comparing the calculations using the full SDPF model space with the truncated SDF calculations. Looking first at the $E2$ properties, it is apparent from the $\beta_Q^{\rm th}$ values that excitations into the $p_{3/2}f_{5/2}p_{1/2}$ shell are needed to produce significant prolate deformations in ^{38}S and ^{40}S. Furthermore, in ^{40}S, the quadrupole moment and $B(E2)$ are not consistent with the same intrinsic quadrupole deformation unless the neutrons can occupy the $p_{3/2}f_{5/2}p_{1/2}$ shell. Inspection of the wavefunctions indicates that the development of quadrupole collectivity depends most sensitively upon the occupation of the $\nu p_{3/2}$ orbit.

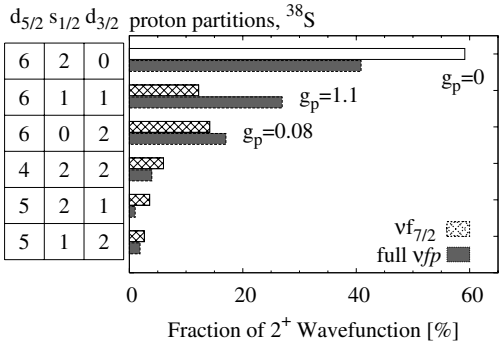

Fig. 9. Dominant proton partitions in ^{38}S comparing calculations in which neutrons occupy the full pf shell (SDPF) with calculations in which they are restricted to the $f_{7/2}$ shell (SDF). The g factors which represent the diagonal contributions of the most important configurations are indicated.

This development of quadrupole collectivity can be linked to the quasi-$SU(3)$ symmetry identified by Zuker et al. [35] and considered for the sulfur isotopes by Retamosa et al. [34]. In the neutron space the $\Delta j = 2$ orbits $f_{7/2}p_{3/2}$, which develop a quasi-$SU(3)$ symmetry, are important. In the proton space the important orbits driving quadrupole collectivity are the $d_{3/2}$ and $s_{1/2}$ orbits, which approximate the geometry of pseudo-$SU(3)$. Furthermore, these proton and neutron configurations are strongly coupled, as is evident from the behavior of the g factors. For example, the SDPF and SDF calculations for ^{38}S show a dramatic change in the g factor due to a relatively small occupation of the neutron $p_{3/2}$ orbit: the theoretical g factor moves from -0.358 to -0.003, falling short of the experimental value by a small margin compared with the distance traveled. The changes in the wavefunction that are responsible for this change in the g factor are illustrated in figure 9, which shows how the proton partition of the wavefunction for ^{38}S changes significantly with the occupation of the $p_{3/2}f_{5/2}p_{1/2}$ shell. The striking feature is the significant increase in the contribution of the proton $s_{1/2}d_{3/2}$ configuration, which has a large g factor.

In contrast, for ^{40}S the calculated g factor in the truncated SDF space is similar to that in the full SDPF space and the proton $s_{1/2}d_{3/2}$ configuration contributes strongly

to the wavefunction whether excitations across the $N = 28$ gap are allowed or not. Apparently the effect of a single neutron occupying the $p_{3/2}$ orbit is diluted when three remain in the $f_{7/2}$ shell, and the proton-neutron interactions are such that the increased occupation of the $f_{7/2}$ orbit (alone) gives a prominence to the proton $s_{1/2}d_{3/2}$ configuration. The gap between the effective single particle energies of the proton $d_{3/2}$ and $s_{1/2}$ orbits is known to narrow as neutrons are added to the $f_{7/2}$ shell [36].

In summary, the measured g factors in ^{38}S and ^{40}S support the shell model description of these nuclei. The observed quadrupole collectivity is better interpreted in terms of the symmetries of the shell model Hamiltonian, rather than in terms of hydrodynamical collective models, which fail to explain the g factors.

4 Outlook

Experiments are in progress at HRIBF to calibrate and comprehend the RIV interaction. While the technique is most suited to studies on even-even nuclei, future possibilities include measurements on odd-A nuclei, including Coulomb excited levels built on isomeric states in the beam. Along with Coulomb excitation, transfer reactions on radioactive beams have also shown pronounced azimuthal angular correlations [37], which give scope for future applications of the technique.

The HVTF technique can be applied to measure the g factors of excited states that live about 5 ps or longer, however for heavier nuclei with $Z > 20$ the strength of the transient field at high velocities is not well known. Future work will develop this technique and apply it to study neutron-rich nuclei in the $N = 40$ region.

We are grateful to our many colleagues who contributed to the success of these experiments, especially to our co-authors on [1,2]. The NSCL-based research was supported by NSF grant no PHY-01-10253. AES acknowledges travel support from the Joint Institute for Heavy Ion Research, Oak Ridge, Tennessee and the ANSTO AMRF scheme (Australia).

References

1. N.J. Stone et al., Phys. Rev. Lett. **94**, 192501 (2005)
2. A.D. Davies et al., Phys. Rev. Lett. **96**, 112503 (2006)
3. G. Goldring, in *Heavy Ion Collisions*, Vol. 3, edited by R. Bock (North-Holland, Amsterdam, 1982), p. 484
4. A.E. Stuchbery, A.N. Wilson, P.F. Mantica, Phys. Rev. C **71**, 047302 (2005)
5. G. Kumbartzki et al., Phys. Lett. B **591**, 213 (2004)
6. www.phy.ornl.gov/hribf/equipment
7. A.E. Stuchbery, Nucl. Phys. A **723**, 69 (2003)
8. A.E. Stuchbery, Computer code CHAD (unpublished)
9. A. Winther, J. de Boer, in *Coulomb Excitation*, edited by K. Alder, A. Winther (Academic Press, New York, 1966), p. 303
10. A.E. Stuchbery et al. (in preparation)
11. A.E. Stuchbery, N.J. Stone (in preparation)
12. G. Jakob et al., Phys. Rev. C **65**, 024316 (2002)
13. B.A. Brown et al., Phys. Rev. C **71**, 044317 (2005)
14. J. Terasaki, J. Engel, W. Nazarewicz, M. Stoitsov, Phys. Rev. C **66**, 054313 (2002)
15. N. Shimizu, T. Otsuka, T. Mizusaki, M. Honma, Phys. Rev. C **70**, 054313 (2004)
16. D. Bazzacco et al., Nucl. Phys. A **533**, 541 (1991)
17. J. Holden et al., Phys. Rev. C **63**, 024315 (2001)
18. J.M. Brennan, M. Hass, N.K.B. Shu, N. Benczer-Koller, Phys. Rev. C **21**, 574 (1980)
19. M. Sambataro, A.E.L. Dieperink, Phys. Lett. B **107**, 249 (1981)
20. A.E. Stuchbery, Phys. Rev. C **69**, 064311 (2004)
21. A.E. Stuchbery et al., Phys. Rev. C **74**, 054307 (2006)
22. E.A. Stefanova et al., Phys. Rev. C **72**, 014309 (2005)
23. S. Schielke et al., Phys. Lett. B **571**, 29 (2003)
24. M.J. Taylor et al., Phys. Lett. B **559**, 187 (2003)
25. B.A. Brown et al., *Oxbash for Windows PC*, Michigan State University, Report No. MSU-NSCL 1289 (2004)
26. S. Nummela et al., Phys. Rev. C **63**, 044316 (2001)
27. E. Caurier et al., Rev. Mod. Phys. **77**, 427 (2005)
28. H. Scheit et al., Phys. Rev. Lett. **77**, 3967 (1996)
29. T. Glasmacher et al., Phys. Lett. B **395**, 163 (1997)
30. J.A. Winger, P.F. Mantica, R.M. Ronningen, M.A. Caprio, Phys. Rev. C **64**, 064318 (2001)
31. D. Sohler et al., Phys. Rev. C **66**, 054302 (2002)
32. R. Rodríguez-Guzmán, J.L. Edigo, L.M. Robledo, Phys. Rev. C **65**, 024304 (2002)
33. E. Caurier, F. Nowacki, A. Poves, Nucl. Phys. A **742**, 14 (2004)
34. J. Retamosa, E. Caurier, F. Nowacki, A. Poves, Phys. Rev. C **55**, 1266 (1997)
35. A.P. Zuker, J. Retamosa, A. Poves, E. Caurier, Phys. Rev. C **52**, R1741 (1995)
36. T. Otsuka et al., Phys. Rev. Lett. **95**, 232502 (2005)
37. D.C. Radford (private communication)